MATERIALS SCIENCE

A single-phase epitaxially grown ferroelectric perovskite nitride

Songhee Choi[1]†, Qiao Jin[1]†, Xian Zi[2]†, Dongke Rong[1]†, Jie Fang[3], Jinfeng Zhang[3], Qinghua Zhang[1], Wei Li[4], Shuai Xu[1], Shengru Chen[1,5], Haitao Hong[1,5], Cui Ting[1,5], Qianying Wang[1,5], Gang Tang[6], Chen Ge[1], Can Wang[1,5], Zhiguo Chen[1], Lin Gu[4], Qian Li[4], Lingfei Wang[3], Shanmin Wang[7,8]*, Jiawang Hong[2]*, Kuijuan Jin[1,5]*, Er-Jia Guo[1,5]*

The integration of ferroelectrics with semiconductors is crucial for developing functional devices, such as field-effect transistors, tunnel junctions, and nonvolatile memories. However, the synthesis of high-quality single-crystalline ferroelectric nitride perovskites has been limited, hindering a comprehensive understanding of their switching dynamics. Here we report the synthesis and characterizations of epitaxial single-phase ferroelectric cerium tantalum nitride ($CeTaN_3$) on both oxides and semiconductors. The polar symmetry of $CeTaN_3$ was confirmed by observing the atomic displacement of central ions relative to the center of the TaN_6 octahedra, as well as through optical second harmonic generation. We observed switchable ferroelectric domains using piezoresponse force microscopy, complemented by the characterization of square-like polarization–electric field hysteresis loops. The remanent polarization of $CeTaN_3$ reaches approximately 20 microcoulomb per square centimeter at room temperature, consistent with theoretical calculations. This work establishes a vital link between ferroelectric nitride perovskites and their practical applications, paving the way for next-generation information and energy storage devices.

INTRODUCTION

Integration with silicon is pivotal for the practical implementation of ferroelectrics (*1*–*5*). This integration offers dual benefits: First, it allows for the amalgamation of polarized state switching with the well-understood electrical characteristics of silicon, including high mobility, tunable carrier density, and chemical stability (*6*, *7*). These hybrid structures unlock enhanced functionalities beyond what silicon alone can achieve. Second, this integration is compatible with complementary metal-oxide semiconductor technology, enabling the utilization of existing infrastructure, cost reduction, and acceleration of device and technology developments (*8*, *9*). Presently, the integration of ferroelectric functionalities in close proximity to silicon relies on perovskite and binary oxides (*10*–*13*). There is a compelling need to explore other inorganic oxygen-free ferroelectric materials that exhibit comparable ferroelectric properties.

In contrast to perovskite oxides, there have been relatively few reports on nitride perovskites. As shown in Fig. 1A, $ThTaN_3$ was the first theoretically predicted and experimentally discovered nitride perovskites, dating back to 1995 (*14*). $ThTaN_3$ powder was synthesized by reacting oxide precursors under a nitrogen-rich environment at high temperatures ranging from 1100° to 1500°C. Following this pioneering work, there was a hiatus in the exploration of nitride perovskites due to synthesis challenges and the lack of remarkable physical properties in the initial precursor. Recently, many theoretical groups have revisited nitride perovskites and predicted that several of these materials may exhibit excellent ferroelectric and piezoelectric properties (*15*–*18*). For instance, Sarmiento-Pérez *et al.* (*15*) used high-throughput calculations to predict numerous thermodynamically stable and experimentally accessible nitride perovskites. Among these, lanthanum tungsten nitride ($LaWN_3$) was identified as a potential ferroelectric semiconductor with a distorted perovskite structure in its ground state. An experimental study by Talley *et al.* (*19*) reported that $LaWN_3$ polycrystalline thin films exhibit a polar structure and piezoelectric response comparable to oxides. Shortly thereafter, a group of nitride perovskites ($CeMoN_3$, $CeWN_3$, and etc.) was theoretically predicted and experimentally achieved; in particular, $CeTaN_3$ was firstly predicted by Ha *et al.* (*20*, *21*). They used magnetron sputtering and N_2 annealing process to fabricate phase-pure Ce-based nitride perovskites that exhibit interesting optoelectronic responses and low-temperature magnetic behaviors. This pioneer work initiated research on nitride perovskites, making them a material system as important as perovskite oxides and other functional materials.

The field of functional nitride perovskites research remains largely uncharted, and the recent experimental breakthrough challenges the focus on superior piezoelectric properties solely within oxides, sparking increased interest in nitride materials with a perovskite structure. The simplistic framework of the perovskite crystal structure enables the possibility of epitaxial growth of nitride perovskites on conventional oxide substrates, with (pseudo-)cubic lattice constants ranging from 3.8 to 4.2 Å (*22*). An even more exciting aspect is that the experience in the oxide interface engineering can be readily applied to the research of nitride perovskites. Simultaneously, the industry has developed mature techniques for integrating perovskite or binary oxides with silicon substrates, offering an opportunity to integrate nitride perovskites as well. This integration could have a

---

[1]Beijing National Laboratory for Condensed Matter Physics and Institute of Physics, Chinese Academy of Sciences, Beijing 100190, China. [2]School of Aerospace Engineering, Beijing Institute of Technology, Beijing 100081, China. [3]Hefei National Research Center for Physical Sciences at Microscale, University of Science and Technology of China, Hefei 230026, China. [4]School of Materials Science and Engineering, Tsinghua University, Beijing 100084, China. [5]Department of Physics and Center of Materials Science and Optoelectronics Engineering, University of Chinese Academy of Sciences, Beijing 100049, China. [6]Beijing Institute of Technology, Zhuhai Beijing Institute of Technology (BIT), Zhuhai 519088, China. [7]Department of Physics, Southern University of Science and Technology, Shenzhen 518055, China. [8]Quantum Science Center of Guangdong-Hongkong-Macao Greater Bay Area, Shenzhen, Guangdong, 518045, China.
*Corresponding author. Email: kjjin@iphy.ac.cn (K.J.); wangsm@sustech.edu.cn (S.W.); hongjw@bit.edu.cn (J.H.); ejguo@iphy.ac.cn (E.-J.G.)
†These authors contributed equally to this work.

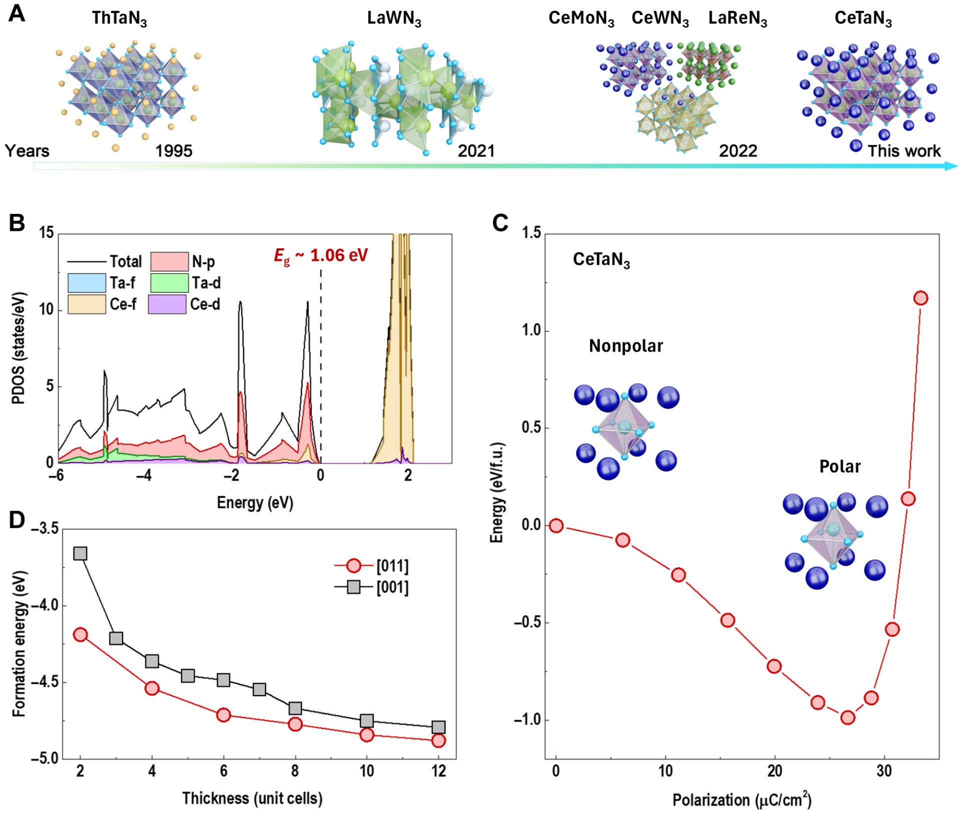

Fig. 1. Theoretically predicted stable nitride perovskites. (**A**) Theoretical and experimental biography of nitride perovskites (ABN_3) from the first discovery of $ThTaN_3$ to this work. (**B**) The total and projected density of states (PDOS) of $CeTaN_3$ calculated using DFT. The conduction bands are mainly occupied by Ce 4f electrons, whereas the valence bands are dominated by N 2*p* electrons. (**C**) The free energy of strained $CeTaN_3$ thin films as a function of calculated ferroelectric polarization. The valley trend confirms that the $CeTaN_3$ thin films can be stabilized in a ferroelectric polar structure. (**D**) Comparison of formation energies of (001)- and (011)-oriented $CeTaN_3$ with different film thicknesses.

profound impact on both fundamental research and applied technologies in the future.

While the initial demonstration of polar nitride perovskites showcases a piezoelectric character suitable for capacitors and actuators, its micrometer thickness and polycrystalline nature now restrict broader applications in ferroelectric devices (*19*, *23*). Ideally, the high-quality single-crystalline thin films are preferred. The influence of grain boundaries is largely removed, resulting in the reduced leakage current and fast-switching dynamics (*24*, *25*). Still, there are limited attempts for exploring the single-crystalline nitride perovskites thin films due to the difficulty in the synthesis. To fabricate the high-quality and correct stoichiometric nitride perovskites with negligible defects remains highly challenging, not to mention the integration with a wide range of oxide and semiconductor substrates.

In this study, we synthesized the single-crystalline thin films of cerium tantalum nitride ($CeTaN_3$). Multiple techniques and electrical measurements were used to confirm the polar structural symmetry and ferroelectric nature of $CeTaN_3$. At room temperature, its remnant polarization was found to be comparable to that of hafnium zirconium oxide and barium titanate, in good agreement with our first-principles calculations. The successful integration of high-quality perovskite nitride thin films on both oxide and semiconductor substrates underscores the potential of the broader nitride perovskites family. With its superior functionalities, this family emerges as a promising counterpart to the well-studied oxide, halide, and chalcogenide perovskites (*26*–*28*).

RESULTS

Growth of high-quality single-phase $CeTaN_3$ thin films

The main challenge in stabilizing nitride perovskites is compensating for the three nitrogen ions (N^{3-}) to achieve a collective anion valence of −9, which must match the collective cation valence of A^{4+} and B^{5+} (or A^{3+} and B^{6+}) in the composition of ABN_3. Earlier work by Ha *et al.* (*20*) computationally screened all possible nitride perovskites through comprehensive ab initio calculations, theoretically predicting $CeTaN_3$ as a stable semiconductor. Thus, we started from performing the first-principles calculations based on density functional theory (DFT) to compute the density of states (DOS) (Fig. 1B) and the minimized energy of its polar structure (Fig. 1C). The detailed band structure is provided in fig. S1. The band structures indicate that $CeTaN_3$ is a semiconductor with indirect bandgap of 1.06 eV. We observed that the top of the valence band mainly arises from the orbital hybridization of Ce *f* and N *p* orbitals, while the Ce *f* orbitals also contribute to the bottom of the conduction band. With suitable substrate selection or cation doping, the bandgap of $CeTaN_3$ can be tuned by altering its phase and symmetry

(*20*). Its relatively small bandgap allows absorption in the infrared and visible spectral range, making it a promising candidate for optoelectronic applications. Using DFT calculations, we further explored the evolution of the bandgap in $CeTaN_3$ as a function of biaxial strain (figs. S2 and S3). With increasing compressive strain, the bandgap widens due to the upward shift of the conduction band. To predict the possible ferroelectric structures of $CeTaN_3$, we had performed calculations for all space groups that meet the requirements of point group 4*mm* (based on the follow-up experimental results), and only *P*4*mm* was found to be stable. We investigated the energy stability of $CeTaN_3$ films with both centrosymmetric nonpolar structures (P4/*mmm* phase) and polar structures (P4*mm* phase). The polar and nonpolar structures are depicted in Fig. 1C. The ferroelectricity of tetragonal $CeTaN_3$ was demonstrated along the ferroelectric switching path from the nonpolar phase to the polar phase. We present the calculated double well energy profiles as a function of calculated polarization, with energy barriers of ~0.9 eV/formula unit, yielding to a large remnant polarization of ~26.6 μC/cm^2. The calculation results indicate that the ferroelectricity in $CeTaN_3$ is driven by the orbital hybridization of A-site cations and *p* orbitals of anions. This result is consistent with ferroelectrics that have lone pair electrons, such as $PbTiO_3$ and $BiFeO_3$, although $CeTaN_3$ does not have lone pair electrons. Similar hybridization is also observed in other ferroelectric nitride perovskites (*14*–*18*), which contrasts with ferroelectric perovskite oxides without lone pair electrons, where ferroelectricity originates from the hybridization of *d* orbitals of cations and *p* orbitals of oxygen ions. We calculated the formation energies, cleavage energies, and surface energies of bulk $CeTaN_3$ with different crystallographic orientations (Fig. 1D and fig. S4). The notably low formation energy and strong stability, attributed to the harmonious coexistence of Ce^{4+} and Ta^{5+} oxidation states, suggest the feasibility of synthesizing $CeTaN_3$ single crystals via physical vapor deposition.

We used a high-pressure and high-temperature synthesis approach to preparing a stoichiometric $CeTaN_3$ ceramic target (fig. S5). This method has been effectively adopted in our previous works for various high-quality binary transition metal nitrides (*23*, *29*–*31*) and was described in a recent report on triclinic $LaReN_3$ (*32*). The $CeTaN_3$ target is composed of Ce, Ta, and N with a molar ratio of approximately 1:1:3, as determined by x-ray diffraction (XRD) and energy-dispersive x-ray (EDX) measurements. Initially, we fabricated $CeTaN_3$ thin films on (001)-oriented $SrTiO_3$ single crystal substrates using pulsed laser deposition (PLD). The relatively high vacuum environment together with home-built flowing nitrogen plasma (generation of highly active nitrogen atoms) has largely removed the impact of remaining oxygen atoms during thin-film deposition. The as-grown $CeTaN_3$ films were amorphous and lacked apparent diffraction peaks; however, they became crystallized after a rapid thermal process (RTP) (see Materials and Methods). Previously, the same procedure was used to synthesize crystallized $CeMoN_3$, $CeWN_3$, and $LaWN_3$ films using magnetron sputtering (*19*, *21*). This method was found to effectively eliminate secondary fluorite-type phase. In our work, the slow growth rate by nitrogen plasma–assisted PLD largely preserved the chemical composition of the ceramic target. Postdeposition annealing in flowing ammonia using RTP further facilitated the formation of single-crystalline $CeTaN_3$ thin films while ensuring a pure single-phase perovskite. Following the same procedure, we also grew single-crystalline $CeTaN_3$ thin films on silicon substrates with 10-unit-cell-thick $SrTiO_3$ buffer layers. During the deposition, a 2- to 3-nm-thick amorphous SiO_2 interlayer was naturally formed between the $SrTiO_3$ and silicon substrates (see schematic in Fig. 2A). Infrared absorption spectra of both amorphous and crystallized $CeTaN_3$ films, compared to bare $SrTiO_3$-buffered silicon substrates, were measured (fig. S6). The infrared absorption peak shifted from 300.9 to 263.3 cm^{-1}, as indicated by colored arrows, and the peak intensities at 536.7 and 611.4 cm^{-1} slightly increased after crystallization. These peak shifts after crystallization suggest reduced phonon scattering in the crystallized $CeTaN_3$ films.

Structural characterizations of high-quality single-crystalline $CeTaN_3$ thin films

The structure of $CeTaN_3$ thin films on (001)-oriented $SrTiO_3$ and $SrTiO_3$/Si substrates were examined by XRD and scanning transmission electron microscopy (STEM) (figs. S7 to S10). Figure 2B shows the XRD θ-2θ scans of $CeTaN_3$ thin films. The $CeTaN_3$ thin films are (00*l*)-oriented without other impurity peaks. The sharp diffraction peaks with clear Laue oscillations (inset of Fig. 2B) demonstrate the high crystallinity of $CeTaN_3$. The thickness of $CeTaN_3$ thin films is ~80 nm, determined from x-ray reflectivity measurements. The phi-scans around the 022 reflection of the $CeTaN_3$ films and 011 reflection of the Si substrates were measured (fig. S11). The results validate that the $CeTaN_3$ thin film was epitaxially grown on Si substrates with a 45° rotation along the surface normal, consistent with previous reports of perovskite oxides directly grown on silicon substrates (*33*). Analysis of the reciprocal space mapping (RSM) in Fig. 2C confirms that the $CeTaN_3$ films were epitaxially grown on silicon substrates. The $CeTaN_3$ film peak exhibits a slight shift to a lower q_x position compared to that of the silicon substrates, indicating that the $CeTaN_3$ films are not fully strained and have slightly relaxed lattice constants. The RSM around the 013 reflection shows a single peak, indicating that the $CeTaN_3$ films show a uniform single domain. We further determined that the $CeTaN_3$ films have a tetragonal-like structure with lattice constants $a = b = 4.03$ Å and $c = 4.09$ Å (fig. S12). Note that the tetragonality of $CeTaN_3$ films on Si substrates is slightly increased compared to the $CeTaN_3$ films grown directly on $SrTiO_3$ substrates. The chemical composition of $CeTaN_3$ thin films was determined by x-ray photoelectron spectroscopy (XPS) measurements (fig. S13). The single oxidation states of Ta^{5+} and N^{3-} ions were confirmed, while the main peaks are attributed to Ce^{4+} with a minor presence of Ce^{3+}, likely due to inevitable small amount of nitrogen vacancies or dislocations present in $CeTaN_3$ surface layers. The occupied electronic state around the Fermi level for $CeTaN_3$ on $SrTiO_3$/Si were taken from XPS valence band spectra (fig. S14). The DOS across the Fermi level matches well with the insulating behavior of $CeTaN_3$ films. The broad peak around 4 to 8 eV is mostly formed by N 2*p* bands and hybridized bands between cations and nitrogen ions. The obtained bandgap of $CeTaN_3$ thin films is ~1.27 eV. In addition, we performed optical absorption spectroscopy measurements (fig. S14). The results show that the absorption coefficient (α) is proportional to $(\hbar\omega - E_g)^2$, indicating that $CeTaN_3$ is an indirect bandgap semiconductor. The extracted optical bandgap is ~1.16 eV, consistent with our former theoretical calculations (Fig. 1B). To assess the chemical uniformity of $CeTaN_3$ thin films, we performed time-of-flight secondary ion mass spectrometry (ToF-SIMS) measurements. The results confirm the uniformity of all deposited layers and provide insight into the chemical distribution from top to bottom (fig. S15).

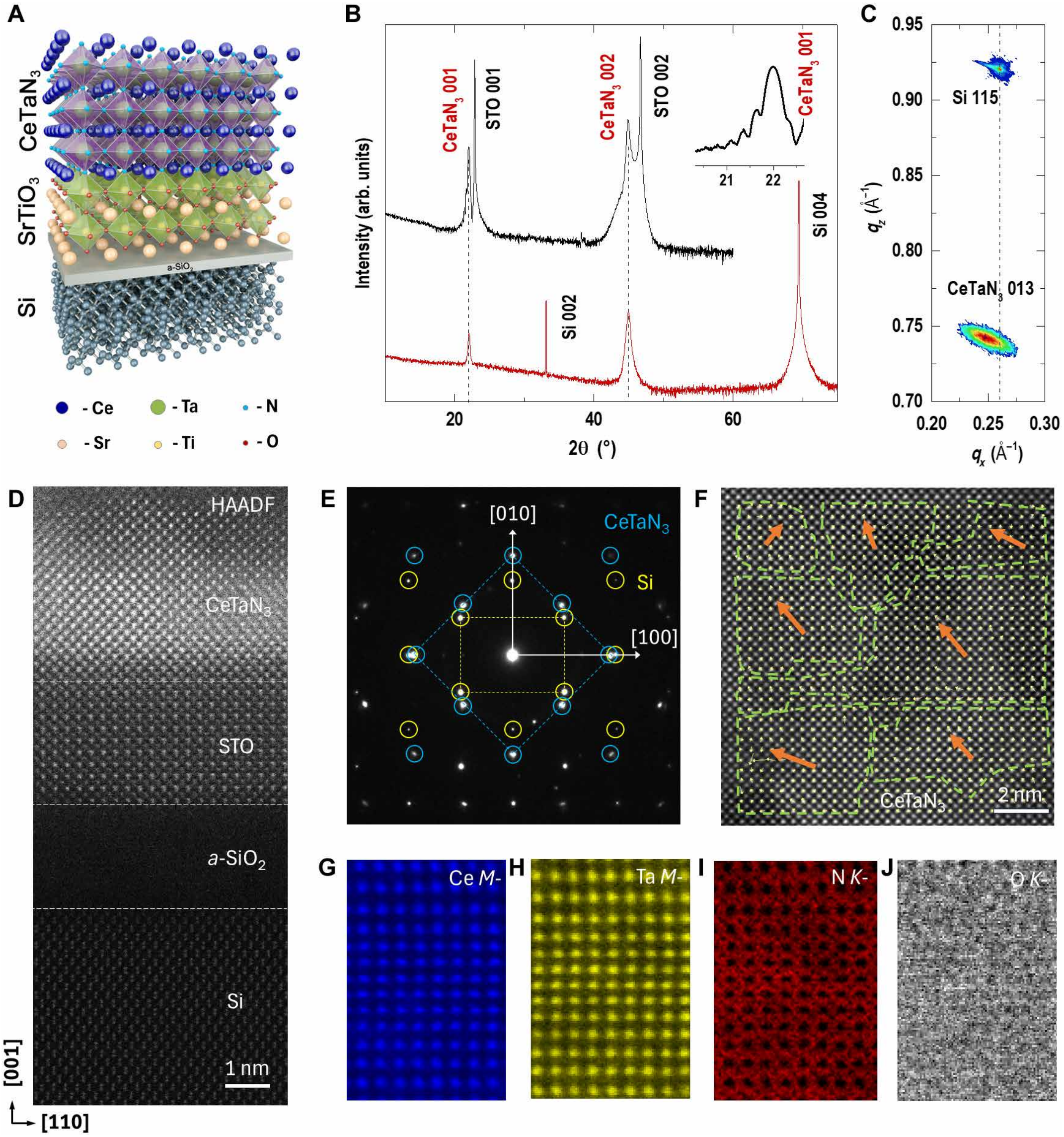

Fig. 2. High-quality single-crystalline $CeTaN_3$ thin films. (**A**) Schematics of $CeTaN_3/SrTiO_3/a\text{-}SiO_2/Si$ substrates. An ultrathin amorphous Si was formed under the growth conditions. The unit cells of $CeTaN_3$, $SrTiO_3$, and Si were identified. (**B**) XRD θ-2θ scans of $CeTaN_3$ on $SrTiO_3$ and $SrTiO_3/Si$ substrates containing an inset figure of zoom-in $CeTaN_3$ 001 diffraction peak with clear Laue oscillations. (**C**) RSM of $CeTaN_3$ 013 around the reflection of Si 115. (**D**) High-resolution high-angle annular dark-field (HAADF)–scanning transmission electron microscopy (STEM) image and (**E**) corresponding SAED pattern of $CeTaN_3/SrTiO_3/a\text{-}SiO_2/Si$. Blue and yellow circles identify the electron diffractions from $CeTaN_3$ and Si, respectively. (**F**) HAADF-STEM image of a representative region from single-crystalline $CeTaN_3$. The orange arrows indicate the cation displacement vectors of central Ta ions in each unit cell. (**G** to **J**) Compositional EELS mapping taken simultaneously at Ce *M*-, Ta *M*-, N *K*-, and O *K*-edges, respectively.

The atomic-scale structural coherency was examined by high-angle annular dark-field (HAADF) and annular bright-field (ABF) imaging taken in STEM mode. High-resolution cross-sectional STEM image of $CeTaN_3/SrTiO_3/a\text{-}SiO_2/Si$ was viewed along silicon substrate's [110] and [010] orientations (Fig. 2D and fig. S16). These images demonstrate the epitaxial growth of $CeTaN_3$ thin films with chemically sharp and coherent interfaces (indicated by yellow dashed lines). The selected area electron diffraction (SAED) pattern was acquired from the interface region, as shown in Fig. 2E. There are two series of sharp and periodic diffraction spots from SAED patterns. In the cross-sectional view, the blue circled peaks ($CeTaN_3$) show a square, while the yellow circled peaks (Si) represent a rectangle with long transverse than longitudinal in the reciprocal space. We found the out-of-plane $CeTaN_3$ [010] || Si [010] alignment and in-plane $CeTaN_3$ [100] || Si [100] alignment. To characterize the chemical composition of $CeTaN_3$, the STEM electron energy lose spectra (EELS) at a representative region in $CeTaN_3$ were measured. Figure 2 (G to I) shows the atomical positions of each Ce, Ta, and N atoms with chemical compositions. From STEM-EELS results, we could clearly identify the perovskite structure of $CeTaN_3$ and uniformed chemical distribution. Figure 2J shows the close-to-background signal from O *K*-edges, suggesting the extremely low concentration of oxygen in $CeTaN_3$ films. The crystal homogeneity of $CeTaN_3$ was confirmed in expanded atomic-resolution STEM images (Fig. 2F and fig. S17). The local polarization within the $CeTaN_3$ lattice can be quantitatively determined on the basis of the displacement of TaN_6 octahedral relative to the center of the TaN_6 octahedral (*34*). The $CeTaN_3$ films show typical polar domains with displacement vectors pointing toward the same direction. The typical polar domain structures with diameters of tens of micrometers and domain volume fraction of ~70%. The dashed regions indicate the polar domains within the $CeTaN_3$ films. The polarization of domains points toward upward with both in-plane and out-of-plane vectors for the intrinsic states. Please note that the films are not completely polarized by electric field, meaning that the observed polar domains are the imprints within the films. Therefore, the polarization is supposed to be relatively smaller than the polarized states. Figure S18 shows the ABF image of $CeTaN_3$ films acquired in the same region. The Ta atoms were shifted from the center of TaN_6 octahedra, resulting in polar symmetry breaking. We extracted that the averaged displacement of Ta atoms is 12.1 ± 1.3 pm from the center of the TaN_6 octahedral along the [001] orientation from the cubic center. Thus, from the atomic displacement, we calculated that the ferroelectric polarization of $CeTaN_3$ is ~20 to 25 $\mu C/cm^2$ using the Born effective charges.

Confirmation of polar structure and switchable piezoresponse in $CeTaN_3$

We conducted second harmonic generation (SHG) measurements on $CeTaN_3$ thin films grown on $SrTiO_3$/Si substrates to shed light on the structural origin of ferroelectrics (see setup in Fig. 3A). This technique is a sensitive probe for the structure symmetry and polar nature. Figure 3B shows the experimental data and theoretical fits to the SHG intensity $I^{2\omega}_{P-\mathrm{out}}$ and $I^{2\omega}_{S-\mathrm{out}}$. We verified that $CeTaN_3$ films have a *P*4*mm* space group, exhibiting stable polar symmetry character. In contrast, the amorphous $CeTaN_3$ films do not show apparent SHG signals. The uniformity of polar domains was examined using lateral SHG mapping (Fig. 3C). The brightness of SHG image represents higher SHG intensity, i.e., larger polarization. The $CeTaN_3$ films exhibit bright SHG signal spots randomly distributed with

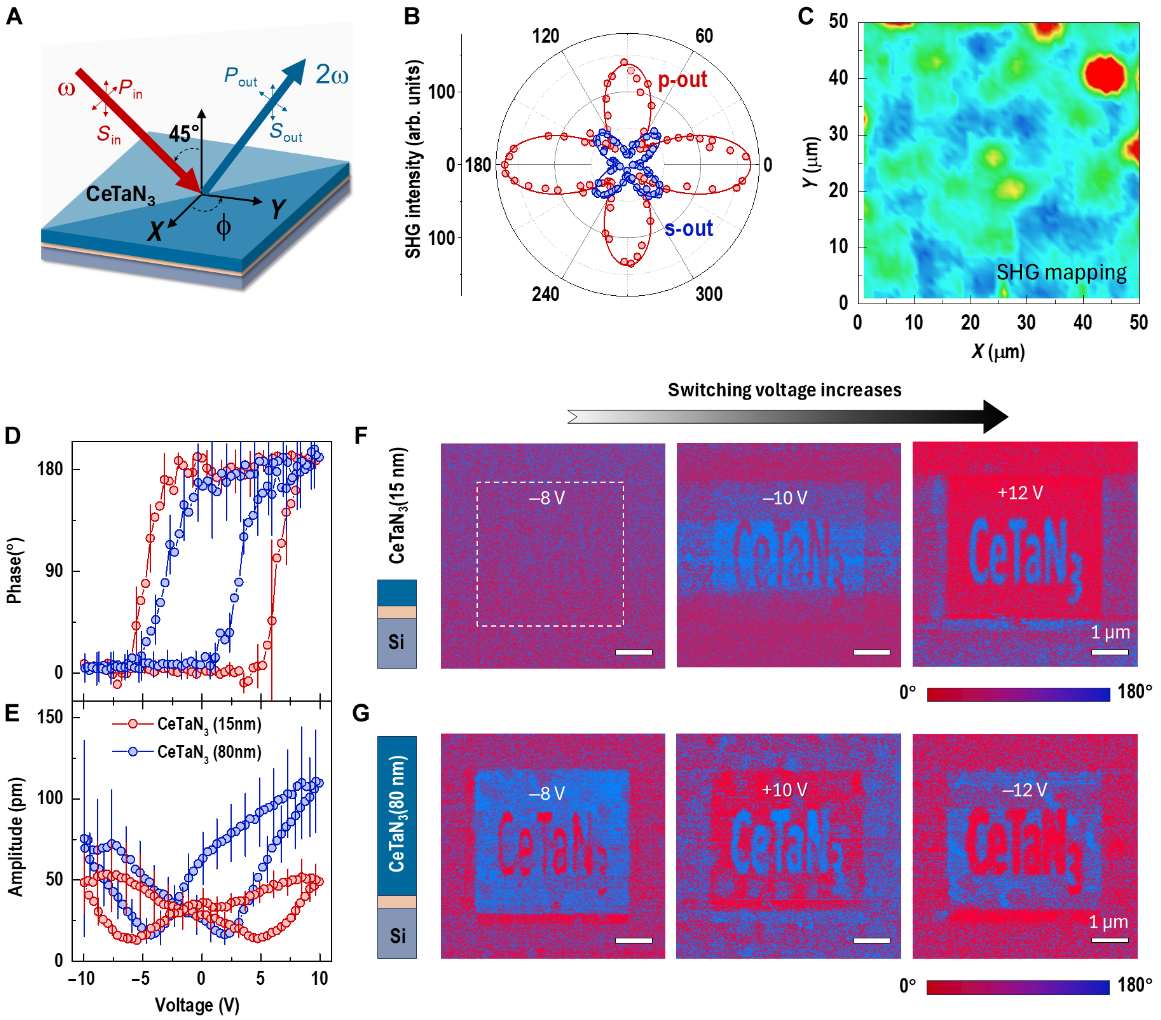

Fig. 3. Switchable polar structure of $CeTaN_3$ thin films confirmed by SHG and PFM. (**A**) Schematic of SHG setup. (**B**) SHG results of 2ω responses. (**C**) SHG mapping conducted over an area of 50 μm by 50 μm on an $CeTaN_3$ thin film. (**D**) PFM phase and (**E**) PFM amplitude hysteresis loops from a 15-nm-thick and an 80-nm-thick $CeTaN_3$ thin films, respectively. PFM phase images of (**F**) a 15-nm-thick and (**G**) an 80-nm-thick $CeTaN_3$ thin films with progressively increasing switching voltages. A square area was switched uniformly, and then the characters $CeTaN_3$ were written with opposite tip voltages.

clear boundaries. Apparently, the ferroelectric domains are unevenly distributed over a 50 μm–by–50 μm region, in agreement with previous STEM observations. The size of polar domains is approximately in the micrometer scale.

The macroscopic analysis for polarization symmetry breaking and electrical piezoresponse of $CeTaN_3$ was conducted with piezoresponse force microscopy (PFM). Figure 3 (D and E) displays the local piezoelectric hysteresis loops as a function of tip voltage in both phase and amplitude signals, respectively. A 15-nm-thick $CeTaN_3$ film exhibits polarization switching at ~±5 V, while the switching voltages decrease for an 80-nm-thick $CeTaN_3$ film. Notably, we observed asymmetric switching voltages in the thicker $CeTaN_3$ films (+2 V for downward switching and −4.4 V for upward switching). The increased coercive field in thinner ferroelectric films arises from the increase nucleation energy barrier and enhanced depolarization field. In addition, the piezoresponse amplitude increases with film thickness. Figure 3 (F and G) shows PFM phase images from the 15-nm-thick and 80-nm-thick $CeTaN_3$ films, respectively, with full sets of PFM amplitude and phase images provided in figs. S19 and S20. To conduct the measurements, the sample was first poled with a fixed tip voltage over a large square area of 4 μm by 4 μm. Then, the characters "$CeTaN_3$" were written using the same tip voltage but with opposite polarity. The switching voltages progressively increased from left to right. For the 15-nm-thick $CeTaN_3$ film, no stable domain could be written at a tip voltage below 8 V, possibly due to unswitchable domains at low fields or domain relaxation between writing and reading. Clear written domains were observed after increasing the tip voltage to 12 V. The same procedure was repeated on the 80-nm-thick $CeTaN_3$ film, and because of its lower switching field, stable written domains appeared even at ±8 V. It is noteworthy that the domain size, i.e., the width of the written characters, increased with higher switching voltages—a common phenomenon in ferroelectric oxides, where domain walls expand laterally faster at higher tip voltages and fixed duration time (scanning speed). All measurements were repeated with reversibly switched tip voltages at multiple positions on the film surface. The written domain patterns remained clearly identifiable after several weeks, confirming the nonvolatile nature of the switchable domains.

Universal synthesis procedure for single-crystalline $CeTaN_3$ films on semiconductors

To demonstrate the universal synthesis procedure, we fabricated $CeTaN_3$ films directly on Si substrates, as well as on other third-generation semiconductor substrates, including SiC and GaN (Fig. 4, A to C). As shown in Fig. 1D, the formation energy of (011)-oriented $CeTaN_3$ is lower than that of (001)-oriented $CeTaN_3$. Therefore, in the absence of substrate regulation, the $CeTaN_3$ films preferentially crystallize along the (011) orientation. Figure 4E displays the XRD θ-2θ scans of $CeTaN_3$ thin films on different substrates. Only (0*ll*) peaks from $CeTaN_3$ and peaks from the substrates (indicated by "*") were observed. A direct comparison with $CeTaN_3$ single-crystalline thin films grown on (011)-oriented $SrTiO_3$ substrates confirms that the (011)-oriented $CeTaN_3$ films were epitaxially grown on all substrates. Microstructural analysis further confirms the epitaxial growth of $CeTaN_3$ thin films on various substrates (figs. S21 and S22). Because of the base pressure of the high-temperature PLD growth chamber reaching only $\sim 1 \times 10^{-8}$ torr, oxidation of the Si substrate was unavoidable, leading to the formation of an ultrathin SiO_2 layer, ~1 nm thick, between the $CeTaN_3$ film and the Si substrate (fig. S21). In addition, detailed EDX mapping of a $CeTaN_3$ film grown on Si (fig. S23) shows uniform distribution of Ce, Ta, and N signals within the films, with no apparent oxygen content detected. Chemical intermixing at the $CeTaN_3$/Si interface was negligible.

Figure 4F presents a representative STEM-ABF image of (011)-oriented $CeTaN_3$ films, where the light dark spots correspond to N atoms. The in-phase rotation along the [001] orientation (*b* axis) allows for direct visualization and quantification of TaN_6 octahedral tilts in the *ac*-plane. The Ta-N-Ta bond angle ($\beta_{\text{Ta-N-Ta}}$) reaches ~158°, and the TaN_6 octahedra tilt is ~11°. The octahedral tilt remains nearly constant within the observed region. This small tilt angle may result from substrate-induced compressive strain. To examine the effects of misfit strain on the tilt angle, we fabricated $CeTaN_3$ thin films on various oxide substrates with progressively decreasing in-plane lattice constants (figs. S24 and S25). Our results show that the $\beta_{\text{Ta-N-Ta}}$ angle decreases with increasing compressive strain, consistent with previous studies on oxide heterostructures. The EELS mapping results for a $CeTaN_3$ thin film on $DyScO_3$ (fig. S26) reveal exceptionally high chemical homogeneity, with minimal intermixing at the heterointerface, confined to a single unit cell. The pristine interface between the nitride perovskite and oxide is attributed to their chemical stability, structural compatibility, and well-defined interface termination, exemplified by the TaN_2-DyO configuration at the $CeTaN_3/DyScO_3$ interface.

The piezoresponse of $CeTaN_3$ thin films on Si was confirmed by poling quadratic areas using oppositely written voltages (fig. S27). Macroscopic electric measurements were conducted at room temperature. Figure 4G shows the electrical hysteresis loops (*P-E* and *J-E* curves) of a Pt/$CeTaN_3$/*p*-Si capacitor. The Pt/Ti top electrode area was reduced to 5 μm in diameter to minimize leakage current to the order of submicroamperes. The remanent polarization (P_r) and the coercive field (E_C) of $CeTaN_3$ films are ~17.4 $\mu C/cm^2$ and 484 kV/cm, respectively. To confirm the intrinsic ferroelectric nature of $CeTaN_3$ thin films, we performed positive-up-negative-down measurements (fig. S28) and calculated the switched polarization under different writing pulses (fig. S29). The switching current varies with the applied electric field and writing time. The characteristic switching time was determined to be $\sim 1 \times 10^{-4}$ s at 667 kV/cm. The higher fields accelerating ferroelectric domain switching, where the smaller fields decrease the ferroelectric switching and lead to incomplete domain switching when fields below E_C (fig. S30). Please note that both P_r and switching speed are comparable to those of typical ferroelectric oxides (such as $Hf_{1-x}Zr_xO_2$ and $BaTiO_3$) (*35*, *36*). The E_C of $CeTaN_3$ films is also comparable to those of the conventional ferroelectric perovskite oxides (*37*–*39*), atomically thin binary oxides (*40*), two dimensional materials (*41*), and elementary substances (*42*). Further investigations into the scaling of ferroelectric parameters with respect to thickness/orientation and switching dynamics in both microscopic scales are essential for advancing the potential of $CeTaN_3$ in ferroelectric applications with semiconductor industry in future.

DISCUSSION

In conclusion, we have successfully achieved the single-crystalline ferroelectric $CeTaN_3$ thin films on silicon substrates, demonstrating the potential for realizing comparable ferroelectric polarization in nitride perovskites. The spontaneous remanent polarization and intrinsic ferroelectric atomic displacement within the TaN_6 octahedra

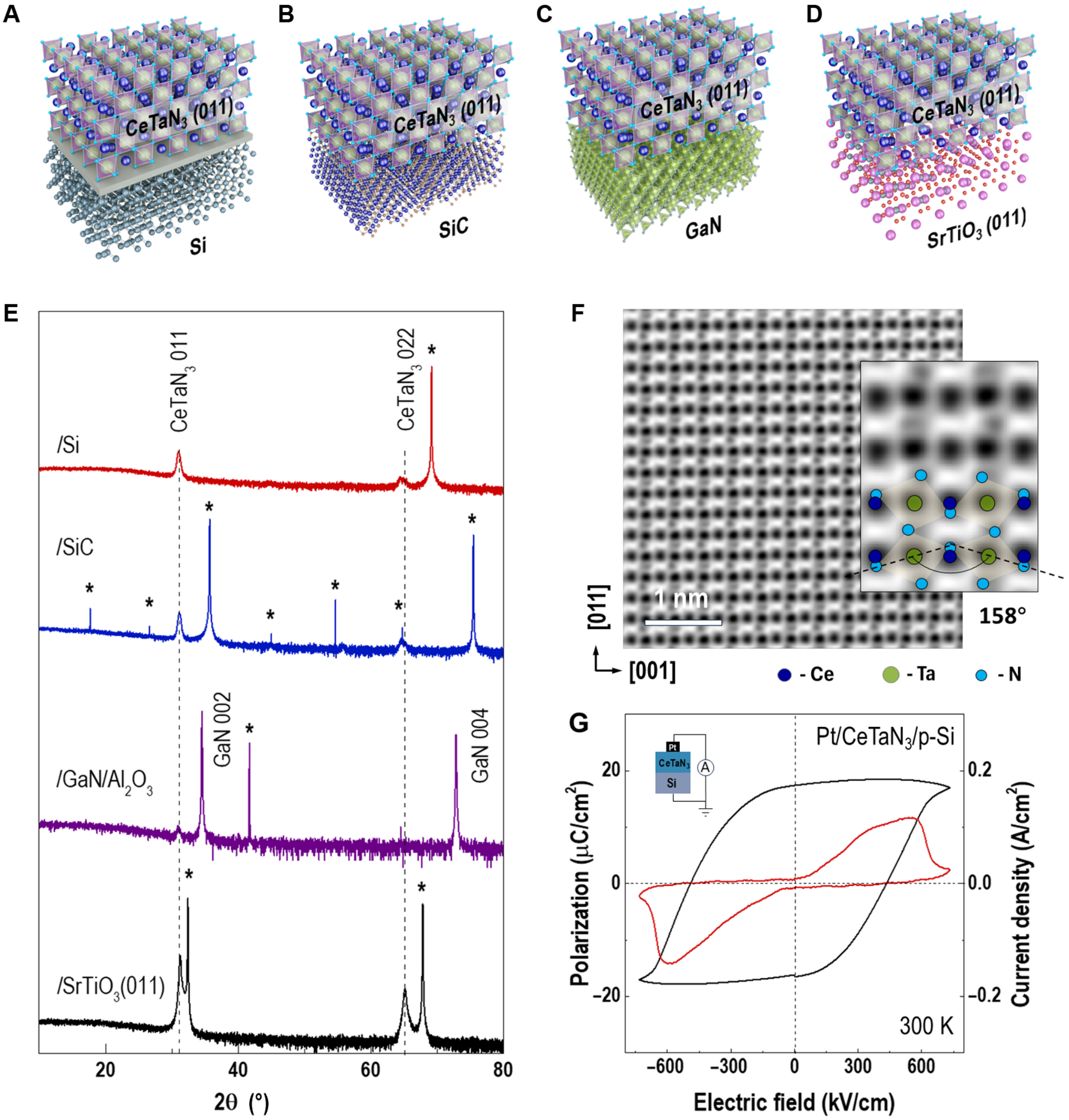

Fig. 4. Naturally formed (011)-oriented $CeTaN_3$ thin films on wide-range semiconductors. (**A** to **D**) Schematics of (011)-oriented $CeTaN_3$ thin films grown on Si, SiC, GaN/Al_2O_3, and (011)-oriented $SrTiO_3$ substrates, respectively. (**E**) XRD θ-2θ scans of $CeTaN_3$ thin films on various substrates (indicated with *). Dashed lines indicate the positions of (0*ll*) peaks from $CeTaN_3$ thin films. (**F**) High-magnified STEM-ABF image from a (011)-oriented $CeTaN_3$ thin film grown on Si. Inside shows a representative tilted TaN_6 octahedral with an averaged Ta-N-Ta bond angle of ~158°. (**G**) Ferroelectric hysteresis loops and switching currents of a $Pt/CeTaN_3/p$-Si capacitor. The measurements were conducted at room temperature. Inset shows the schematic of measurement setup.

reveal a strong correlation between the electronic structure and inversion symmetry. The experimentally observed ferroelectric order parameters align excellently with theoretical calculations. The clear observation of nitrogen octahedral tilting in nitride perovskites highlights the sensitivity of nitrogen octahedra to epitaxial strain. Fine-tuning of octahedral parameters—such as rotation, bond angles, and bond lengths—could enable quantum confinements of their emergent physical properties. In addition, the similarity in octahedral engineering between oxide and nitride perovskites suggests that combining these materials could open a largely unexplored research avenue at the oxide/nitride interfaces. Our work also emphasizes the potential for integrating single-crystalline $CeTaN_3$ thin films with second- and third-generation semiconductor substrates, as well as perovskite oxide substrates. This integration enhances the advantages of this ferroelectricity in nitride perovskites, not only in fundamental research but also for next-generation artificial intelligence–driven computing and memory devices. Furthermore, we noticed that a recent publication reported that the Ruddlesden-Popper nitrides, specifically Ce_2TaN_4, were synthesized under high pressure (*43*). This compound exhibited long-range order in charge distribution, off-center displacement, octahedral tilting, and spin states, suggesting that this material system holds potential as a functional nitride. Consequently, the exploration of not only single-crystalline perovskite nitrides but also Ruddlesden-Popper nitrides—and a broader array of nitride materials—remains an exciting frontier for future research.

MATERIALS AND METHODS

$CeTaN_3$ target preparation and thin-film growth

Polycrystalline $CeTaN_3$ serves as ablation target with 25 mm in diameter and 5 mm in thickness. The target was sintered at 3 GPa and 1000°C for 60 min, using the single-phase perovskite nitride powders as starting materials. The nitride powders were synthesized though a recently formulated high-pressure reaction route. High-pressure experiments were carried out in a Duanzao Suo 6 × 10 meganewtons cubic press installed at the High-Pressure Lab of Southern University of Science and Technology (SUSTech). The $CeTaN_3$ target was used to fabricate the thin films using PLD system with a XeCl excimer laser of 308-nm wavelength and 5-Hz repetition. The laser spot size is ~5.5 mm^2, and the energy density maintains ~1 J/cm^2 during the deposition. We used highly active nitrogen atom generator-nitrogen plasma to compensate the nitrogen vacancies during the deposition. The (001)- and (011)-oriented $SrTiO_3$, (001)-oriented $LaAlO_3$, (110)-oriented $DyScO_3$, and *n*-type Si, SiC, and GaN/Al_2O_3 single crystals were used as substrates. A 5-nm-thick $SrTiO_3$ buffer layer was prepared on Si substrates using two-step methods which described in our previous works (*44*–*46*). The $CeTaN_3$ thin films were prepared in two steps. First, the as-grown stoichiometric films were deposited at the substrate temperature of 600°C and the base pressure of 1×10^{-8} torr. The thickness of $CeTaN_3$ thin films was controlled by counting the number of laser pulses. The second step was to anneal the films using RTP, which is crucial for crystalizing the $CeTaN_3$ thin films. The annealling process was performed by heating up the films to 800°C in 10 min under pure anomia atmosphere. After 30-min annealling, the films cooled down to room temperature slowling.

Structure characterizations

The thin-film quality was examined by high-resolution four-circle x-ray diffractometer (Malvern Panalytical, X'Pert3 MRD) and synchrotron-based XRD at the beamline 1W1A of the Beijing Synchrotron Radiation Facility (BSRF). The θ-2θ line scans, rocking curve scans, φ scans, and off-specular RSM were conducted to check the epitaxial growth of $CeTaN_3$ thin films. The atomic structure of $CeTaN_3$ thin films were characterized using an ARM-200CF scanning transmission electron microscope which was operated at 200 keV and was equipped with double spherical aberration (Cs) correctors. The STEM spicemen were prepared by standard mechanical thinning followed by ion milling. All TEM images were processed and analyzed using Gatan DigitalMicrograph.

ToF-SIMS measurements

ToF-SIMS measurements were carried out using a ToF-SIMS (ION-TOF GmbH, M6 instrument, Münster, Germany). The mass spectrometer was equipped with a reflection type ToF analyzer. A dual-beam depth profiling strategy was used, in which a 1-keV Ar ion gun (300 μm–by–300 μm scanning area) was used for sputtering and a 30-keV Bi_3^+ beam (~0.43 pA, 100 μm–by–100 μm scanning area within the center of the Cs+ crater) was used for negative spectra data collection with high mass resolution mode. In addition, a flood gun (~1 μA) was used for charge compensation. The $CeTaN_3$film/$SrTiO_3$/Si substrate interfaces were determined via the secondary ion signals of SrO^+ and Sr^{4+}.

Optical reflectance measurements

The optical reflectance measurements in the energy range of 10 to 1000 meV were performed on a Bruker Vertex 80v Fourier transform spectrometer at room temperature. The transmitance spectra of amorphous and crystallized $CeTaN_3$ thin films on $SrTiO_3$-capped Si substrates were measured, in comparison to that of a bare $SrTiO_3$-capped Si substrates. The optical transmitance data were highly reproducble. Moreover, the optical constants of the $CeTaN_3$ thin films were obtained using a ellipsometer (J.A. Woollam RC2 spectroscopy), which are consistent with the results extracted from the measured reflectance spectra in the same energy range.

Optical SHG

Optical SHG measurements were performed on two independent home-developed systems. For the point SHG measurements, we performed at the Institute of Physics, Chinese Academy of Sciences (CAS). A Ti:sapphire femtosecond laser (Tsunami 3941-X1BB, Spectra-Physics) with a pulse duration of 120 fs, a center wavelength of 800 nm, and an average power of 50 to 200 mW was used as the light source. The 1ω laser beam was incident on the $CeTaN_3$ thin films with an angle of 45°, while the 2ω signals in the reflected laser beam were band-pass filtered and recorded with a photodetector. For the SHG mapping measurements, the experiment was conducted at Tsinghua University using a laser scanning microscope system. We used a normal incidence geometry. The 1ω laser beam was focused by an objective lens and scanned with a pair of galvanometers. The backscattered 2ω light signals were collected from reflection beam using a photomultiplier tube. In both cases, the polarization of incident beam was controlled with a zero-order half-wave plate, and the polarization of the SHG light was analyzed using a Glan-Taylor prism. The intensities of *p*- and *s*-polarized SHG light were plotted as a function of beam polarization, i.e., the angle with respect to beam. All SHG measurements were performed at room temperature.

Ferroelectric characterizations

PFM was conducted using an atomic force microscopy (AFM) from Asylum Research Company (type: MFP-3D family) at room temperature. A Si cantilever with conductive Pt/Ir coating layer of spring constant of 0.2 N/m was used. Both amplitude and phase signals were recorderd. The dc bias voltages were applied from 4 to 12 V for switching ferroelectric domains. Ferroelectric polarization measurements have been conducted with an Aixacct TF 2000 Analyzer on $CeTaN_3$ thin-film capacitor structures with Pt top electrodes with an area as small as 25-μm^2 area to largely reduce the leakage current.

X-ray photoelectron spectroscopy

Room temperature XPS measurements were performed at the Institute of Physics, CAS. All XPS measurements were measured with x-rays at a normal angle to the sample surface. The samples were chemically cleaned to remove the surface contaminations. Spectra were measured using an electron flood gun to compensate the positive photoemission charge because $CeTaN_3$ thin films were highly insulating. A small polycrystalline Au foil was affixed to the corner of each film surface using Cu tape to connect the sample to the ground. For valence band spectra, the Au $4f_{7/2}$ peak was used to calibrate the binding energy scale. The distribution of element valence states was obtained by fitting N 2*p* XPS using the Casa XPS software.

DFT calculations

The calculations were performed in the framework of DFT as implemented in the Vienna ab initio simulation package code (*47*, *48*).

The electron exchange-correlation effects were treated with the generalized gradient approximation with Perdew-Burke-Ernzerhof solid functional (*49*, *50*). The Heyd-Scuseria-Ernzerhof functional was applied for the calculation of the DOS (*49*). Energy convergence can be further confirmed by using a cutoff energy of 500 eV and a *k*-point grid with a reciprocal space resolution of 0.2 $Å^{-1}$. The in-plane lattice constant was fixed to the experimental values during relaxation, while the out-of-plane lattice constant and atomic position were fully relaxed. The PSEUDO program from the Bilbao Crystallographic Server was used to identify the centrosymmetric structure (*51*–*53*), while the VTST code was used to obtain the insert structures along ferroelectric switching path from nonpolar phase to polar phase (*54*, *55*).

Supplementary Materials

This PDF file includes:

Figs. S1 to S30
References

REFERENCES AND NOTES

1. R. A. McKee, F. J. Walker, M. F. Chisholm, Crystalline oxides on silicon: The first five monolayers. *Phys. Rev. Lett.* **81**, 3014–3017 (1998).
2. A. Pasquarello, M. S. Hybertsen, R. Car, Interface structure between silicon and its oxide by first-principles molecular dynamics. *Nature* **396**, 58–60 (1998).
3. M. P. Warusawithana, C. Cen, C. R. Sleasman, J. C. Woicik, Y. Li, L. F. Kourkoutis, J. A. Klug, H. Li, P. Ryan, L.-P. Wang, M. Bedzyk, D. A. Muller, L.-Q. Chen, J. Levy, D. G. Schlom, A ferroelectric oxide made directly on silicon. *Science* **324**, 367–370 (2009).
4. S. H. Baek, J. Park, D. M. Kim, V. A. Aksyuk, R. R. Das, S. D. Bu, D. A. Felker, J. Lettieri, V. Vaithyanathan, S. S. N. Bharadwaja, N. Bassiri-Gharb, Y. B. Chen, H. P. Sun, C. M. Folkman, H. W. Jang, D. J. Kreft, S. K. Streiffer, R. Ramesh, X. Q. Pan, S. Trolier-McKinstry, D. G. Schlom, M. S. Rzchowski, R. H. Blick, C. B. Eom, Giant piezoelectricity on Si for hyperactive MEMS. *Science* **334**, 958–961 (2011).
5. S. K. Lee, B. H. Choi, D. Hesse, Epitaxial growth of multiferroic $BiFeO_3$ thin films with (101) and (111) orientations on (100) Si substrates. Epitaxial growth of multiferroic $BiFeO_3$ thin films with (101) and (111) orientations on (100) Si substrates. *Appl. Phys. Lett.* **102**, 242906 (2013).
6. M. Suzuki, Review on future ferroelectric nonvolatile memory: FeRAM. *J. Cerma. Soc. Jpn.* **103**, 1099–1111 (1995).
7. P. Vettiger, G. Binnig, The Nanodrive Project. *Sci. Am.* **288**, 46 (2003).
8. A. L. Esaki, R. B. Laibowitz, P. J. Stiles, Polar switch. *IBM Tech. Discl. Bull* **13**, 2161 (1971).
9. Y.-R. Wu, J. Singh, Polar heterostructure for multifunction devices: Theoretical studies. *IEEE Trans. Electron Devives* **52**, 284–293 (2005).
10. S. S. Cheema, D. Kwon, N. Shanker, R. dos Reis, S.-L. Hsu, J. Xiao, H. Zhang, R. Wagner, A. Datar, M. R. McCarter, C. R. Serrao, A. K. Yadav, G. Karbasian, C.-H. Hsu, A. J. Tan, L.-C. Wang, V. Thakare, X. Zhang, A. Mehta, E. Karapetrova, R. V. Chopdekar, P. Shafer, E. Arenholz, C. Hu, R. Proksch, R. Ramesh, J. Ciston, S. Salahuddin, Enhanced ferroelectricity in ultrathin films grown directly on silicon. *Nature* **580**, 478–482 (2020).
11. S. S. Cheema, N. Shanker, L.-C. Wang, C.-H. Hsu, S.-L. Hsu, Y.-H. Liao, M. S. Jose, J. Gomez, W. Chakraborty, W. Li, J.-H. Bae, S. K. Volkman, D. Kwon, Y. Rho, G. Pinelli, R. Rastogi, D. Pipitone, C. Stull, M. Cook, B. Tyrrell, V. A. Stoica, Z. Zhang, J. W. Freeland, C. J. Tassone, A. Mehta, G. Saheli, D. Thompson, D. I. Suh, W.-T. Koo, K.-J. Nam, D. J. Jung, W.-B. Song, C.-H. Lin, S. Nam, J. Heo, N. Parihar, C. P. Grigoropoulos, P. Shafer, P. Fay, R. Ramesh, S. Mahapatra, J. Ciston, S. Datta, M. Mohamed, C. Hu, S. Salahuddin, Ultrathin ferroic HfO_2-ZrO_2 superlattice gate stack for advanced transistors. *Nature* **604**, 65–71 (2022).
12. S. S. Cheema, N. Shanker, S.-L. Hsu, Y. Rho, C.-H. Hsu, V. A. Stoica, Z. Zhang, J. W. Freeland, P. Shafer, C. P. Grigoropoulos, J. Ciston, S. Salahuddin, Emergent ferroelectricity in subnanometer binary oxide films on silicon. *Science* **376**, 648–652 (2022).
13. K. J. Hubbard, D. G. Schlom, Thermodynamic stability of binary oxides in contact with silicon. *J. Mater. Res.* **11**, 2757–2776 (1996).
14. N. E. Brese, F. J. DiSalvo, Synthesis of the first thorium-containing nitride perovskite, $TaThN_3$. *J. Solid State Chem.* **120**, 378–380 (1995).
15. R. Sarmiento-Pérez, T. F. T. Cerqueira, S. Körbel, S. Botti, M. A. L. Marques, Prediction of stable nitride perovskites. *Chem. Mater.* **27**, 5957–5963 (2015).
16. Y.-W. Fang, C. A. J. Fisher, A. Kuwabara, X.-W. Shen, T. Ogawa, H. Moriwake, R. Huang, C.-G. Duan, Lattice dynamics and ferroelectric properties of the nitride perovskite $LaWN_3$. *Phys. Rev. B* **95**, 014111 (2017).
17. C. Gui, J. Chen, S. Dong, Multiferroic nitride perovskites with giant polarizations and large magnetic moments. *Phys. Rev. B* **106**, 184418 (2022).
18. X. Zi, Z. Deng, L. Rao, Y. Li, G. Tang, J. Hong, J., First-principles study of ferroelectric, dielectric, and piezoelectric properties in the nitride perovskites Ce BN_3(B = Nb, Ta). *Phys. Rev. B* **109**, 115125 (2024).
19. K. R. Talley, C. L. Perkins, D. R. Diercks, G. L. Brennecka, A. Zakutayev, A., Synthesis of $LaWN_3$ nitride perovskite with polar symmetry. *Science* **374**, 1488–1491 (2021).
20. V.-A. Ha, H. Lee, F. Giustino, $CeTaN_3$ and $CeNbN_3$: Prospective nitride perovskites with optimal photovoltaic band gaps. *Chem. Mater.* **34**, 2107–2122 (2022).
21. R. Sherbondy, R. W. Smaha, C. J. Bartel, M. E. Holtz, K. R. Talley, B. Levy-Wendt, C. L. Perkins, S. Eley, A. Zakutayev, G. L. Brennecka, High-throughput selection and experimental realization of two new Ce-based nitride perovskites: $CeMoN_3$ and $CeWN_3$. *Chem. Mater.* **34**, 6883–6893 (2022).
22. A. Biswas, C.-H. Yang, R. Ramesh, Y. H. Jeong, Atomically flat single terminated oxide substrate surfaces. *Prog. Surf. Sci.* **92**, 117–141 (2017).
23. X. Zhou, W. Xu, Z. Gui, C. Gu, J. Chen, J. Xie, X. Yao, J. Dai, J. Zhu, L. Wu, E.-j. Guo, X. Yu, L. Fang, Y. Zhao, L. Huang, S. Wang, Polar nitride perovskite $LaWN_{3-δ}$ with orthorhombic structure. *Adv. Sci.* **10**, 2205479 (2023).
24. P. Gao, C. T. Nelson, J. R. Jokisaari, S. H. Baek, C. W. Bark, Y. Zhang, E. Wang, D. G. Schlom, C. B. Eom, X. Pan, Revealing the role of defects in ferroelectric switching with atomic resolution. *Nat. Commun.* **2**, 591 (2011).
25. E.-J. Guo, R. Roth, A. Herklotz, D. Hesse, K. Dörr, K., Ferroelectric 180° domain wall motion controlled by biaxial strain. *Adv. Mater.* **27**, 1615–1618 (2015).
26. S. Geng, Z. Xiao, Can nitride perovskites provide the same superior optoelectronic properties as lead halide perovskites? *ACS Energy Lett.* **8**, 2051–2057 (2023).
27. E. Aydin, T. G. Allen, M. D. Bastiani, A. Razzaq, L. Xu, E. Ugur, J. Liu, S. D. Wolf, Pathways toward commercial perovskite/silicon tandem photovoltaics. *Science* **383**, 6679 (2024).
28. B. F. Grosso, D. W. Davies, B. Zhu, A. Walsh, D. O. Scanlon, Accessible chemical space for metal nitride perovskites. *Chem. Sci.* **14**, 9175–9185 (2023).
29. Q. Jin, H. Cheng, Z. Wang, Q. Zhang, S. Lin, M. A. Roldan, J. Zhao, J.-O. Wang, S. Chen, M. He, C. Ge, C. Wang, H.-B. Lu, H. Guo, L. Gu, X. Tong, T. Zhu, S. Wang, H. Yang, K.-j. Jin, E.-J. Guo, Strain-mediated high conductivity in ultrathin antiferromagnetic metallic nitrides. *Adv. Mater.* **33**, e2005920 (2021).
30. Q. Jin, Z. Wang, Q. Zhang, Y. Yu, S. Lin, S. Chen, M. Qi, H. Bai, A. Huon, Q. Li, L. Wang, X. Yin, C. S. Tang, A. T. S. Wee, F. Meng, J. Zhao, J.-o. Wang, H. Guo, C. Ge, C. Wang, W. Yan, T. Zhu, L. Gu, S. A. Chambers, S. Das, T. Charlton, M. R. Fitzsimmons, G.-Q. Liu, S. Wang, K.-j. Jin, H. Yang, E.-J. Guo, Room-temperature ferromagnetism at an oxide-nitride interface. *Phys. Rev. Lett.* **128**, 017202 (2022).
31. Q. Jin, Q. Zhang, H. Bai, M. Yang, Y. Ga, S. Chen, H. Hong, T. Cui, D. Rong, T. Lin, J.-O. Wang, C. Ge, C. Wang, Y. Cao, L. Gu, G. Song, S. Wang, K. Jiang, Z.-G. Cheng, T. Zhu, H. Yang, K.-j. Jin, E.-J. Guo, Syntropic spin alignment at the interface between ferromagnetic and superconducting nitrides. *Nat. Sci. Rev.* **11**, nwae107 (2024).
32. S. D. Kloß, M. L. Weidemann, J. P. Attfield, Preparation of bulk-phase nitride perovskite $LaReN_3$ and topotactic reduction to $LaNiO_2$ -Type $LaReN_2$. *Angew. Chem. Int. Ed. Engl.* **60**, 22260–22264 (2021).
33. S.-H. Baek, C.-B. Eom, Epitaxial integration of perovskite-based multifunctional oxides on silicon. *Acta Mater.* **61**, 2734–2750 (2013).
34. A. K. Yadav, C. T. Nelson, S. L. Hsu, Z. Hong, J. D. Clarkson, C. M. Schlepütz, A. R. Damodaran, P. Shafer, E. Arenholz, L. R. Dedon, D. Chen, A. Vishwanath, A. M. Minor, L. Q. Chen, J. F. Scott, L. W. Martin, R. Ramesh, Observation of polar vortices in oxide superlattices. *Nature* **530**, 198–201 (2016).
35. J. F. Scott, Applications of modern ferroelectrics. *Science* **315**, 954–959 (2007).
36. K. J. Choi, M. Biegalski, Y. L. Li, A. Sharan, J. Schubert, R. Uecker, P. Reiche, Y. B. Chen, X. Q. Pan, V. Gopalan, L.-Q. Chen, D. G. Schlom, C. B. Eom, Enhancement of ferroelectricity in strained $BaTiO_3$ thin films. *Science* **306**, 1005–1009 (2004).
37. E. J. Guo, K. Dorr, A. Herklotz, Strain controlled ferroelectric switching time of $BiFeO_3$ capacitors. *Appl. Phys. Lett.* **101**, 242908 (2012).
38. Y. Kim, A. Kumar, O. Ovchinnikov, S. Jesse, H. Han, D. Pantel, I. Vrejoiu, W. Lee, D. Hesse, M. Alex, S. V. Kalinin, First-order reversal curve probing of spatially resolved polarization switching dynamics in ferroelectric nanocapacitors. *ACS Nano* **6**, 491–500 (2012).
39. A. Stamm, D. J. Kim, H. Lu, C. W. Bark, C. B. Eom, A. Gruverman, Polarization relaxation kinetics in ultrathin ferroelectric capacitors. *Appl. Phys. Lett.* **102**, 092901 (2013).
40. Q. Yang, J. Hu, Y.-W. Fang, Y. Jia, R. Yang, S. Deng, Y. Lu, O. Dieguez, L. Fan, D. Zheng, X. Zhang, Y. Dong, Z. Luo, Z. Wang, H. Wang, M. Sui, X. Xing, J. Chen, J. Tian, L. Zhang, Ferroelectricity in layered bismuth oxide down to 1 nanometer. *Science* **379**, 1218–1224 (2023).
41. J. Gou, H. Bai, X. Zhang, Y. L. Huang, S. Duan, A. Ariando, S. A. Yang, L. Chen, Y. Lu, A. T. S. Wee, Two-dimensional ferroelectricity in a single-element bismuth monolayer. *Nature* **617**, 67–72 (2023).
42. W. Li, X. Zhang, J. Yang, S. Zhou, C. Song, P. Cheng, Y.-Q. Zhang, B. Feng, Z. Wang, Y. Lu, K. Wu, L. Chen, Emergence of ferroelectricity in a nonferroelectric monolayer. *Nat. Commun.* **14**, 2757 (2023).

43. M. Weidemann, D. Werhahn, C. Mayer, S. Kläger, C. Ritter, P. Manuel, J. P. Attfield, S. D. Kloß, High-pressure synthesis of Ruddlesden-Popper nitrides. *Nat. Chem.* **16**, 1723–1731 (2024).
44. H. Guo, Y. Huang, K. Jin, Q. Zhou, H. B. Lu, L. Liu, Y. Zhou, B. Cheng, Z. Chen, Temperature effect on carrier transport characteristics in $SrTiO_{3-\delta}/Si_{p\text{-}n}$ heterojunction. *Appl. Phys. Lett.* **86**, 123502 (2005).
45. H. F. Tian, H. X. Yang, H. R. Zhang, Y. Li, H. B. Lu, J. Q. Li, Interface of epitaxial $SrTiO_3$ on silicon characterized by transmission electron microscopy, electron energy loss spectroscopy, and electron holography. *Phys. Rev. B* **73**, 075325 (2006).
46. Z. Li, X. Guo, H. B. Lu, Z. Zhang, D. Song, S. Cheng, M. Bosman, J. Zhu, Z. Dong, W. Zhu, An epitaxial ferroelectric tunnel junction on silicon. *Adv. Mater.* **26**, 7185–7189 (2014).
47. P. Hohenberg, W. Kohn, Inhomogeneous electron gas. *Phys. Rev.* **136**, B864–B871 (1964).
48. W. Kohn, L. J. Sham, Self-consistent equations including exchange and correlation effects. *Phys. Rev.* **140**, A1133–A1138 (1965).
49. J. P. Perdew, A. Ruzsinszky, G. I. Csonka, O. A. Vydrov, G. E. Scuseria, L. A. Constantin, X. Zhou, K. Burke, Restoring the density-gradient expansion for exchange in solids and surfaces. *Phys. Rev. Lett.* **100**, 136406 (2008).
50. J. Heyd, G. E. Scuseria, M. Ernzerhof, Hybrid functionals based on a screened Coulomb potential. *J. Chem. Phys.* **118**, 8207–8215 (2003).
51. E. Kroumova, M. I. Aroyo, J. M. Perez-Mato, S. Ivantchev, J. M. Igartu, H. Wondratschek, PSEUDO: A program for a pseudosymmetry search. *J. Appl. Cryst.* **34**, 783–784 (2001).
52. C. Capillas, M. I. Aroyo, J. M. Perez-Mato, Methods for pseudosymmetry evaluation: A comparison between the atomic displacements and electron density approaches. *Z. Krist.* **220**, 691–699 (2005).
53. C. Capillas, E. S. Tasci, G. de la Flor, D. Orobengoa, J. M. Perez-Mato, M. I. Aroyo, A new computer tool at the Bilbao crystallographic server to detect and characterize pseudosymmetry. *Z. Krist.* **226**, 186–196 (2011).
54. D. Sheppard, P. Xiao, W. Chemelewski, D. D. Johnson, G. Henkelman, A generalized solid-state nudged elastic band method. *J. Chem. Phys.* **136**, 074103 (2012).
55. D. Sheppard, G. Henkelman, Paths to which the nudged elastic band converges. *J. Comp. Chem.* **32**, 1769–1771 (2011).
56. A. N. Kolmogorov, Statistical theory of metal crystallization. *Izv. Akad. Nauk SSSR Ser. Math.* **3**, 355 (1937).
57. M. Avrami, Kinetics of phase change. II transformation—time relations for random distribution of nuclei. *J. Chem. Phys.* **8**, 212–224 (1940).

Acknowledgments: We thank Y. Fu, C. Zhou, and X. L. Zhang for preparation of nitride targets at the high-P Lab of SUSTech and X. K. Yao and X. Y. Wang for assistant PFM measurements at IOP-CAS. **Funding:** This work was supported by the Beijing Natural Science Foundation (grant nos. JQ24002 to E.-J.G. and JQ24011 to Q.L.), the National Key Basic Research Program of China (grant no. 2020YFA0309100 to E.-J.G., Q.L., and L.W.), the National Natural Science Foundation of China (grant nos. U22A20263 to E.-J.G., 52250308 to E.-J.G., 12474013 to S.W., 12304158 to Q.J., and 12174175 to L.W.), the CAS Project for Young Scientists in Basic Research (grant no. YSBR-084 to E.-J.G.), the CAS Youth Interdisciplinary Team, the Special Research assistant, the CAS Strategic Priority Research Program (B) (grant no. XDB33030200 to K.J. and E.-J.G.), the Guangdong Basic and Applied Basic Research Foundation (grant no. 2022B1515120014 to E.-J.G.), the Guangdong-Hong Kong-Macao Joint Laboratory for Neutron Scattering Science and Technology, the China Postdoctoral Science Foundation (grant no. 2022M723353 to E.-J.G.), and the International Young Scientist Fellowship of IOP-CAS to S. Choi. XPS experiments were performed at IOP-CAS via a user proposal. The synchrotron-based XRD was conducted at the beamline 1W1A of the BSRF. **Author contributions:** E.-J.G. initiated the research and supervised the work. The perovskite nitride targets were provided by S.W.; the perovskite nitride thin films were grown by S.Cho. and annealed using RTP with guidance from Q.J. and D.R.; TEM lamellas were fabricated with FIB milling, and TEM experiments were performed by Q.Z. and L.G.; XPS measurements were performed by S.Cho., S.Che., H.H., C.T., D.R., and Q.W.; PFM was performed by J.F., J.Z. and L.W.; S.X. and K.J. worked on the SHG point measurements, and W.L. and Q.L. performed on SHG mapping measurements; X.Z., G.T., and J.H. performed the first-principles calculations based on DFT. Z.C. performed the infrared spectroscopy measurements. C.G. and C.W. participated in the discussions and provided suggestions during the manuscript preparation. S.Cho., X.Z., J.H., and E.-J.G. wrote the manuscript with inputs from all authors. **Competing interests:** The authors declare that they have no competing interests. **Data and materials availability:** All data needed to evaluate the conclusions in the paper are present in the paper and/or the Supplementary Materials.

Submitted 16 November 2024
Accepted 9 July 2025
Published 8 August 2025
10.1126/sciadv.adu6698